PAPER

Check for updates

Rational design and synthesis of scintillating lanthanide coordination polymers for highly efficient X-ray imaging†

Xiangmei Liu,[a] Shi Wang,[a] Wangwang Xie,[a] Jingfei Ni,[a] Kang Xiao,[a] Shujuan Liu,[a] Wen Lv [ID] *[a] and Qiang Zhao [ID] *[ab]

Scintillators with high X-ray imaging performance are highly desirable. Traditional inorganic scintillators are restricted by the rigorous preparation conditions and easy deliquescence, while organic scintillators suffered from a low X-ray absorption coefficient and low energy resolution. Metal–organic scintillators were developed to overcome the above-mentioned disadvantages, but they were still limited by the inherent low X-ray attenuation performance of organic ligands and the low energy transfer efficiency between the absorption center and the luminescent center. In this work, two one-dimensional linear lanthanide-based scintillating metal–organic coordination polymers (CPs) were developed by a simple and controllable one-step solvothermal method. High-Z lanthanide atoms could efficiently transform the high-energy X-ray to characteristic visible light *via* the energy bridge effect of organic ligands, which improved the conversion efficiency to enhance light emission. To evaluate the X-ray imaging performance, scintillating CPs were prepared into thin films, which exhibited relatively high spatial resolution. Considering the good X-ray irradiation stability and humidity stability, the lanthanide scintillating CPs are believed to be very promising materials for X-ray imaging.

Introduction

Due to the excellent penetration depth, X-ray imaging has been widely applied in the fields of clinical diagnosis, security, quality inspection and so on.[1,2] The most important core unit for X-ray imaging is scintillator, which could absorb the high-energy X-ray and then transform them to visible light. The performance, components and processing method of scintillators highly affect the imaging quality, detection efficiency, biosafety and costing of X-ray imaging. Commercial scintillators such as NaI:Tl, CsI:Tl and $Bi_4Ge_3O_{12}$ possess a high X-ray absorption coefficient and light yield, while the preparation conditions are usually rigorous and it is not easy to regulate the radiation performances.[3] Compared with the above-mentioned inorganic commercial scintillators, organic scintillators exhibit

the advantages of mild synthesis conditions, modifiable chemical structure and easy processing and show great superiority in flexible X-ray imaging.[4–6] However, the X-ray absorption coefficient and energy resolution of organic scintillators need to be further improved to meet the requirements of low-dose high-resolution X-ray imaging.[6–8]

Recently, metal–organic scintillators (MOSs) such as metal–organic frameworks (MOFs) and metal–organic coordination polymers (CPs)[9–19] have been developed to overcome the limitations of pure inorganic or organic scintillators, which show broad application prospects. The metal centers of MOSs could be high-Z elements such as Pb^{2+},[11,12] Ba^{2+},[10] Hf^{4+} and Zr^{4+}[15,20] to improve the X-ray absorption coefficient. The organic ligands provide flexible chemical structure modification to adjust the energy levels of ligands and further optimize their X-ray excited luminescence properties. Under X-ray irradiation, X-ray photons usually interact with heavy atoms and generate a large number of singlet and triplet excitons in a ratio of 1 : 3 *via* photoelectric effects.[21–24] In this case, the luminescence properties of organic fluorescent chromophores are controlled by the selection rule of electric dipoles, which wastes many triplet excitons, thus resulting in weak X-ray excited luminescence (XEL). To address this problem, strategies of using thermally activated delayed fluorescent (TADF) chromophores or metal ions sensitized by triplet excitons as luminescent centers have

[a] *State Key Laboratory of Organic Electronics and Information Displays, Jiangsu Key Laboratory for Biosensors, Institute of Advanced Materials (IAM), Nanjing University of Posts & Telecommunications, 9 Wenyuan, Nanjing 210023, Jiangsu, P. R. China. E-mail: iamwlv@njupt.edu.cn, iamqzhao@njupt.edu.cn*
[b] *College of Electronic and Optical Engineering & College of Flexible Electronics (Future Technology), Nanjing University of Posts & Telecommunications (NUPT), 9 Wenyuan, Nanjing 210023, P. R. China*
† Electronic supplementary information (ESI) available. CCDC 2243266 and 2259402. For ESI and crystallographic data in CIF or other electronic format see DOI: https://doi.org/10.1039/d3tc00761h

been put forward to harvest triplet excitons.[7,8,16,25,26] For example, the heavy-atom uranium (U) was adopted as a radioluminescence center to synthesise metal–organic complexes, exhibiting highly efficient XEL performance.[17] However, such radioactive element would limit their practical X-ray imaging applications. Therefore, new metal elements should be explored to develop such metal radioluminescence center-based MOSs.

Lanthanide rare earth cations such as Eu^{3+}, Tb^{3+}, Er^{3+} and Dy^{3+} possess relatively high atomic numbers, large Stokes shifts, narrow emission bands, tunable emissions, high emission efficiencies and good photostability,[27–31] which are good candidates for radioluminescence centers. Lanthanide cation-doped inorganic scintillators (*e.g.* lanthanide-doped inorganic oxide-based phosphors or lanthanide-doped fluoride nanomaterials) have been reported.[3,29] However, the lanthanide cation-based metal–organic complexes for X-ray scintillation have been rarely reported. In consideration of the excellent luminescence properties of lanthanide cations and the modifiable chemical structure of organic ligands, scintillators with a high X-ray absorption coefficient and high-efficiency X-ray luminescence could be anticipated. Therefore, the development of lanthanide cation-based MOSs would be very promising and exciting.

In this work, we developed two novel one-dimensional linear metal–organic CPs (Eu-TPC and Tb-TPC) *via* a simple and controllable one-step solvothermal method to achieve high-efficiency X-ray excited luminescence (Fig. 1a and b). The metal radioluminescent center was Eu^{3+} or Tb^{3+}, both of which were excellent luminescent centers in the visible light region. The organic ligand (2,2′:6′,2″-terpyridine-4′-carboxylic acid, TPC) was utilized to bridge the lanthanide cations. Upon X-ray irradiation, X-ray photons first interact with heavy atoms (Eu or Tb) in CPs to generate a large number of high-energy

Fig. 1 (a) Two-dimensional layers and (b) one-dimensional linear topological structures of Eu-TPC and Tb-TPC. (c) Schematic illustration of the energy transfer process of Eu-TPC and Tb-TPC. Ex_{X-ray}: X-ray excitation; Em: emission of lanthanide (Ln^{3+}) cations; ET: energy transfer; S_0: ground singlet state; T_1: first excited triplet state. (d) PXRD patterns and simulated patterns of Eu-TPC and Tb-TPC. (e) Thermogravimetric analysis spectra of Eu-TPC and Tb-TPC.

Professor Dr Wen Lv is currently working in State Key Laboratory of Organic Electronics and Information Displays, School of Chemistry and Life Sciences, Nanjing University of Posts and Telecommunications. She obtained her BSc degree in materials science from Wuhan University of Science and Technology in 2012 and PhD in optical engineering from Nanjing University of Posts and Telecommunications in 2017 under the supervision of Prof. Wei Huang and

Wen Lv

Prof. Qiang Zhao. After conducting postdoctoral research in the University of Hong Kong with Prof. Weiping Wang, she started her independent career at Nanjing University of Posts and Telecommunications in 2021. Her research interests focus on the long-lived excited states in photochemistry and stimuli-responsive materials.

electrons *via* photoelectric effects and Compton scattering. These high-energy hot electrons further interact with atoms in the ligand and lose energy until the ligand molecule is ionized or excited to the excited triplet (T_1) states.[15,21–24] The T_1 energy level of TPC was determined to be 2.61 eV from the phosphorescence emission peak at 475 nm (Fig. S1, ESI†). The T_1 energy level of TPC was higher than the emission states of Eu^{3+} ($^5D_0$, 2.14 eV) and Tb^{3+} ($^5D_4$, 2.54 eV). Thus, energy transfer from the T_1 state of organic ligand (TPC) to lanthanide cations (Eu^{3+} or Tb^{3+}) occurred, resulting in the characteristic emission of lanthanide cations (Fig. 1c). It should be noted that, due to the relatively small energy level difference between Tb^{3+} ($^5D_4$) and T_1 states of TPC (0.07 eV), energy back transfer may occur to slightly decrease the light quantum yield of Tb-TPC,[32] which was also confirmed by the following experimental results. Compared to direct energy conversion from X-ray to visible light in a single lanthanide ion, the proposed strategy utilized organic ligands to act as energy bridges, which improved the conversion efficiency to enhance the characteristic emission of lanthanide cations, providing an effective strategy to develop highly efficient scintillators. Additionally, TPC possesses multiple coordination sites (pyridine and carboxyl) to improve the rigidity of CPs, minimizing non-radiative

transitions to improve the XEL efficiency. Furthermore, Eu-TPC or Tb-TPC microcrystals were mixed with polymethyl methacrylate (PMMA) polymers to prepare flexible scintillating films by a drop-coating method, and the proof of concept of its application in high-resolution X-ray imaging was demonstrated.

Experimental

Materials and methods

Europium(III) nitrate hexahydrate (Eu(NO$_3$)$_3$·6H$_2$O, 99.9%, Aladdin), Terbium(III) chloride hexahydrate (TbCl$_3$·6H$_2$O, 99.9%, Aladdin), 2,2′:6′,2″-terpyridine-4′-carboxylic acid (TPC, 97%, Bidepharm), polymethyl methacrylate (PMMA, average M_w 2 000 000, Aladdin), N,N-dimethylformamide (AR, Sinopharm), chloroform (AR, Sinopharm), and ethanol (AR, Sinopharm) were purchased from commercial sources and used directly without further purification.

The single-crystal structures were characterized using a single-crystal diffractometer (Bruker D8 Quest). The crystallographic data for the structural analysis have been deposited in the Cambridge Crystallographic Data Center with the CCDC reference numbers of 2243266 and 2243267.† The crystalline phases were measured using a X-ray powder diffractometer (Bruker ADVANCE D8) at 40 kV and 20 mA with Cu-K$_\alpha$ radiation (λ = 1.54 Å). The thermal stability was evaluated using a thermogravimetric analyzer (Shimadzu DTG-60). The luminescence spectra were recorded using an Edinburgh FLS-920 spectrometer equipped with a xenon lamp (200 W) as the excitation source. The luminescence lifetimes were determined using an Edinburgh FLS-920 spectrometer equipped with a microflash lamp as the excitation source. The X-ray excited luminescence spectra were recorded using an Edinburgh FLS-920 spectrometer equipped with an X-ray tube (Amptek Mini-X2, Au target, tube voltage 50 kV) as the excitation source. The X-ray dose rates were calibrated using a highly sensitive X-ray ion chamber dosemeter (Radcal Accu-Dose+ 10 × 5–180). The X-ray imaging was conducted using an home-made imaging system constructed by an Au target X-ray tube (Amptek Mini-X2, tube voltage 50 kV) and a digital camera (Nikon 850D).[33] All of the X-ray excited luminescence spectra and X-ray imaging were conducted in a lead box. The X-ray attenuation efficiency, relative light yields and modulation transfer function (MTF) measurements were conducted according to the reported methods.[33,34]

Synthetic procedures

Eu-TPC or Tb-TPC was prepared according to a one-step solvothermal method.[35] In general, TPC (0.05 mmol) was ultrasonic dissolved in 1 mL of N,N-dimethylformamide. After Eu(NO$_3$)$_3$·6H$_2$O or TbCl$_3$·6H$_2$O (0.05 mmol) was ultrasonic dissolved in 1 mL of deionized water, the aqueous solution was mildly added into this TPC solution. The mixture solution was sealed and stored at 100 °C for 24 h. Crystals were generated after reaction, which were washed 3 times with

10 mL of N,N-dimethylformamide, 10 mL of deionized water and 10 mL of ethanol successively. Finally, the crystals were dried at 70 °C for 24 h and then collected for further use.

The flexible scintillating films were prepared by a drop-coating method. The square glass slide (15 × 15 mm), which was ultrasonically washed with acetone, ethanol and deionized water successively, was utilized as a template to prepare scintillating films. The Eu-TPC or Tb-TPC crystals were ground in an agate mortar and then filtrated through a 200 mesh screen to get uniform powders. The poly(methyl methacrylate) (PMMA) (10 mg) was dissolved in 10 mL of chloroform at 80 °C for 30 min. Then, Eu-TPC or Tb-TPC powders were added at a concentration of 30 mg mL^{-1}. The mixture was sonicated for 10 min to prepare a uniform suspension solution. After that, 300 μL of the suspension solution was dripped onto the surface of the square glass slide to form a liquid film, which was further stored at room temperature for drying. The white film was formed on the surface of the glass slide after 24 h, which could be peeled off after placing in deionized water for 10 min. Finally, the white film was dried at room temperature for further use.

Results and discussion

Crystal structure characterizations

The crystal structures of Eu-TPC and Tb-TPC were confirmed by single-crystal X-ray diffraction (SXRD) analysis, which indicated that the CPs crystallized in the monoclinic space group P2$_1$/c (Tables S1 and S2, ESI†). The asymmetry unit of Eu-TPC or Tb-TPC contains one crystallographically independent Ln^{3+} cation, two TPC ligands, one HCOO$^-$ anion and one H$_2$O molecule (Fig. 1b). The HCOO- anion should be generated from the hydrolysis of DMF in the existence of deionized water. Each Ln^{3+} cation was nine-coordinated with three N and six O atoms (Fig. S2, ESI†). The coordination sphere of each Ln^{3+} cation was contributed by three TPC ligands, one HCOO$^-$ anion and one H$_2$O molecule. The Ln^{3+} cations and TPC ligands were alternately arranged linearly, revealing a one-dimensional linear topological structure (Fig. 1b). The neighboring linear chains were further assembled in parallel to form an interdigital structure via π–π interactions and van der Waals interactions (Fig. 1a). The π–π distance between the centers of pyridyl groups on neighboring bridging TPC units was measured to be 3.700 Å and 3.666 Å for Eu-TPC and Tb-TPC, respectively (Fig. S3a, ESI†). The neighboring decorating TPC units exhibited the π–π distances of 3.779 Å and 3.724 Å for Eu-TPC and Tb-TPC, respectively (Fig. S3b, ESI†). The well-stacked TPC enhanced the π–π interactions, promoting electron transfer, energy transfer and crystallization processes. The powder X-ray diffraction (PXRD) patterns of Eu-TPC and Tb-TPC were highly consistent with the simulated XRD patterns (Fig. 1d), which were calculated according to the crystallographic parameters (Tables S1 and S2, ESI†), demonstrating the high purity of the prepared CPs. The thermogravimetric analysis was conducted to assess the thermal stability of Eu-TPC and Tb-TPC. As shown

This journal is © The Royal Society of Chemistry 2023

J. Mater. Chem. C, 2023, 11, 7405–7410 | 7407

in Fig. 1e, little weight loss was observed at a temperature lower than 150 °C, demonstrating good thermal stability in such temperature region. When the temperature increased to 204 °C, the weight loss percentages of Eu-TPC and Tb-TPC were 2.64% and 2.89%, respectively, which was due to the weight loss of a coordinated H_2O molecule (the theoretically calculated values were 2.35% and 2.33%, respectively) and residual solvents, indicating that the coordination structures of Eu-TPC and Tb-TPC were destroyed at such high temperatures.

Photoluminescence properties

The luminescence spectra of Eu-TPC exhibited characteristic emission peaks of Eu^{3+} at wavelengths of 591/596 nm ($^5D_0 \rightarrow {}^7F_1$), 614 nm ($^5D_0 \rightarrow {}^7F_2$), and 685/696 nm ($^5D_0 \rightarrow {}^7F_4$) upon 365 nm light excitation (Fig. 2a).[13,31] The luminescence spectra of Tb-TPC exhibited the characteristic emission peaks of Tb^{3+} at wavelengths of 489 nm ($^5D_4 \rightarrow {}^7F_6$), 542 nm ($^5D_4 \rightarrow {}^7F_5$), 584 nm ($^5D_4 \rightarrow {}^7F_4$), 620 nm ($^5D_4 \rightarrow {}^7F_3$), and 653 nm ($^5D_4 \rightarrow {}^7F_2$) (Fig. 2b).[27] The above-mentioned results indicated that only intense metal-centered emission was found in Eu-TPC and Tb-TPC CPs. The CIE coordinates of Eu-TPC and Tb-TPC were (0.67, 0.33) and (0.34, 0.58), which exhibited red emission and green emission, respectively (Fig. 2c). The photoluminescence quantum yields of Eu-TPC and Tb-TPC were measured to be 42.52% and 16.38%, respectively. The luminescence lifetimes of Eu-TPC and Tb-TPC were measured to be 463 μs and 134 μs, respectively (Fig. 2d), which were suitable for the subsequent studies of scintillation performance.

X-ray excited luminescence properties

The luminescence spectra of Eu-TPC and Tb-TPC upon X-ray excitation also exhibited the characteristic emission peaks of
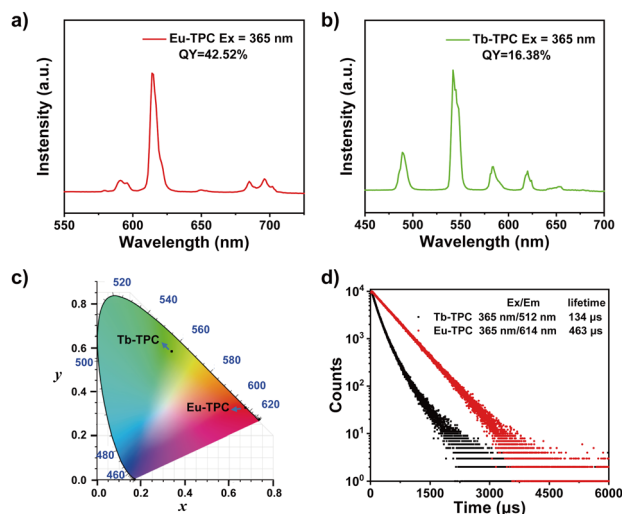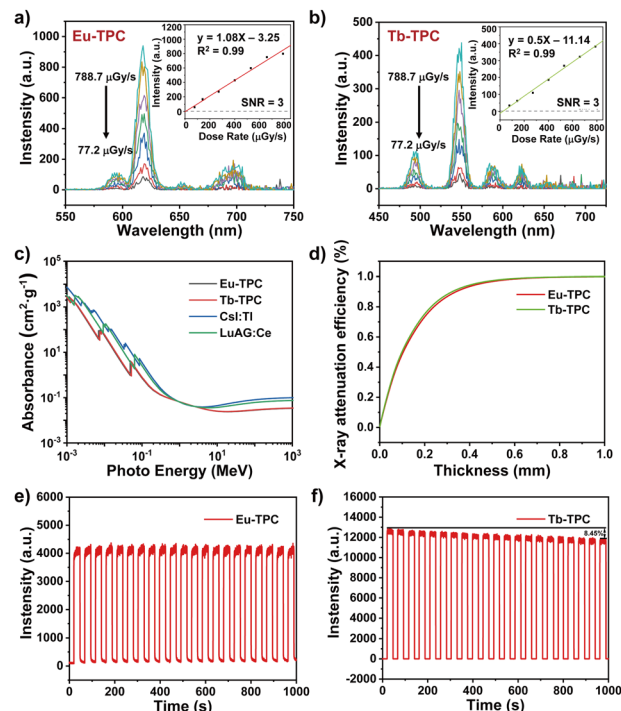

Fig. 3 (a and b) X-ray excited luminescence spectra of Eu-TPC and Tb-TPC in the crystal state at room temperature. Inset: Linear dependence between X-ray excited luminescence intensity and X-ray dose rate at wavelengths of (a) 619 nm and (b) 543 nm. (c) X-ray absorbance of high-energy photons (10^{-3} MeV to 10^3 MeV) of Eu-TPC, Tb-TPC, CsI:Tl and LuAG:Ce. (d) X-ray attenuation efficiencies of Eu-TPC and Tb-TPC films with different thicknesses. (e and f) X-ray irradiation stability of Eu-TPC and Tb-TPC upon X-ray irradiation for 20 cycles (total X-ray dosage was up to 4.51 Gy$_{air}$). X-ray irradiation was switched on for 30 s and then switched off for 20 s in each cycle.

Eu^{3+} and Tb^{3+} cations, respectively, which were similar to the luminescence spectra upon 365 nm light excitation (Fig. 3a and b). With the increase in X-ray dose rate, the luminescence intensity increases linearly. The limit of detection was measured to be 5.2 μGy s^{-1} and 11.14 μGy s^{-1} for Eu-TPC and Tb-TPC, respectively, based on a signal-to-noise ratio at 3. The X-ray absorbance of high-energy photons (10^{-3} MeV to 10^3 MeV) of Eu-TPC and Tb-TPC exhibited the same order of magnitude values as that of the commercial scintillators CsI:Tl and LuAG:Ce (Fig. 3c). The X-ray attenuation efficiencies of Eu-TPC and Tb-TPC films with different thicknesses were also measured, which exhibited 80% of X-ray attenuation efficiencies at thicknesses of 241 μm and 228 μm, respectively (Fig. 3d). The relative light yields of Eu-TPC and Tb-TPC were measured to be 6121 and 5453 photons MeV^{-1}, respectively, by utilizing LuAG:Ce (22 000 photons MeV^{-1}) as the reference.

The X-ray irradiation stability of Eu-TPC and Tb-TPC was investigated by monitoring the luminescence intensity change upon X-ray irradiation for 20 cycles (total X-ray dosage was up to 4.51 Gy$_{air}$) (Fig. 3e and f). The luminescence intensity of Eu-TPC exhibited little degradation after 20 cycles of X-ray irradiation, while the luminescence intensity decreased by 8.5% for Tb-TPC. The PXRD pattern of Eu-TPC and Tb-TPC displayed

Fig. 2 Normalized luminescence spectra of (a) Eu-TPC and (b) Tb-TPC in the crystal state at room temperature. λ_{ex} = 365 nm. (c) CIE 1931 chromaticity coordinates of Eu-TPC and Tb-TPC. (d) Time-resolved luminescent spectra of Eu-TPC and Tb-TPC at room temperature. λ_{ex} = 365 nm.

minimal changes after X-ray irradiation (Fig. S4, ESI†), indicating relatively good X-ray irradiation stability.

X-ray imaging performance

To investigate the X-ray imaging performance, Eu-TPC or Tb-TPC were mixed with poly(methyl methacrylate) (PMMA) to prepare flexible films by a drop-coating method. The X-ray excited luminescence spectra of the films displayed the characteristic emission peaks of Eu^{3+} and Tb^{3+} cations (Fig. 4a). The red and green luminescence could be observed with naked eyes under X-ray irradiation at room temperature, while the pure PMMA film was dark under the same excitation condition. The gray value analysis of the lines, which across the luminescence images of Eu-TPC and Tb-TPC films, exhibited small standard deviation values of 4.24 and 3.79, respectively, demonstrating the good uniformity of the films (Fig. S5, ESI†). The luminescence intensity at the main emission peaks (619 nm for Eu-TPC film and 543 nm for Tb-TPC film) was almost unchanged even though the films were immersed in water for 8 days, indicating good water stability (Fig. S6, ESI†). Good water stability could improve the durability in the normal environment, which is the critical problem that needs to be resolved in the commercial CsI:Tl and perovskite scintillators.[36–38]

The spatial resolution of the films were characterized *via* modulation transfer function (MTF) calculations from the standard X-ray slant edge test, which was conducted by using a thin tungsten slice to acquire X-ray images with sharp edges at a dose rate of 0.18 mGy s^{-1}. At a MTF value of 0.2, the spatial

resolution of Eu-TPC and Tb-TPC films was determined to be 5.15 lp mm^{-1} and 4.46 lp mm^{-1}, respectively (Fig. 4b). The spatial resolution of the films was also evaluated by X-ray imaging of the standard resolution test pattern plate. As shown in Fig. 4c, clear alternately shaded stripes could be observed around the spatial resolution values of 5.5 lp mm^{-1} and 5.0 lp mm^{-1} for Eu-TPC and Tb-TPC films. Compared with the X-ray image of the standard resolution test pattern plate conducted with the Tb-TPC film, the X-ray image conducted with the Eu-TPC film displayed a greater difference between the maximum and minimum gray values at a spatial resolution value of 4 lp mm^{-1}, revealing higher spatial resolution of the Eu-TPC film. This observation was consistent with the MTF calculation results.

The X-ray imaging performance of the films was further evaluated by X-ray imaging of the metallic spring, which was put in a capsule. Due to the different X-ray absorbance between the spring and the capsule, a clear structure of the spring could be observed in the X-ray images (Fig. 4d), demonstrating the excellent X-ray imaging performance of the Eu-TPC and Tb-TPC films.

Conclusions

In summary, a series of one-dimensional linear scintillating lanthanide-organic CPs have been developed by a simple and controllable one-step solvothermal method, which exhibited bright metal-centered luminescence under UV or X-ray irradiation. The lanthanide cations transformed the high-energy X-ray to the characteristic emission light. The organic ligands acted as energy bridges to harvest the X-ray radiation-induced triplet excitons from heavy atoms and then sensitize lanthanide cations for metal-centered XEL. As-obtained Eu-TPC and Tb-TPC demonstrated bright XEL features of Eu^{3+} and Tb^{3+}, excellent linear response to X-ray dose rate and high radiation and humidity stability. The scintillating films containing the CPs were prepared for X-ray imaging, which exhibited relatively high spatial resolution. These results indicated that the rational design of the energy bridge based on organic ligands is a very promising design strategy to develop lanthanide organic CP scintillators for X-ray detection and imaging.

Conflicts of interest

There are no conflicts to declare.
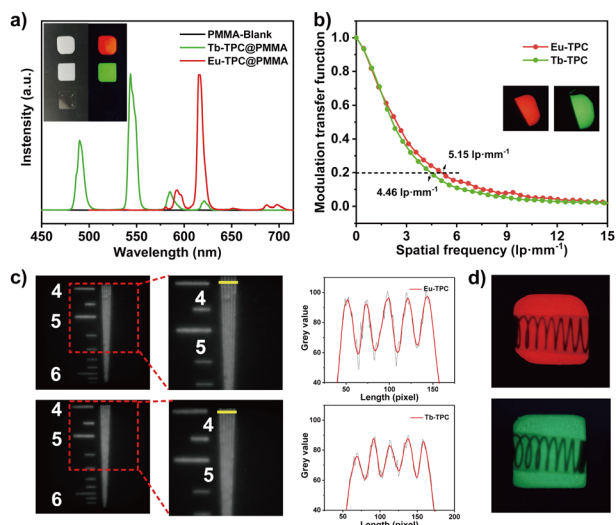
Acknowledgements

Fig. 4 (a) Normalized X-ray excited luminescence spectra of the Eu-TPC film, Tb-TPC film and PMMA film at room temperature. Inset: Digital photographs of the scintillating films at bright field (left column) and under X-ray irradiation (right column). (b) MTF curves of the Eu-TPC film and Tb-TPC film measured by the slanted-edge method. Insets: X-ray images of the Eu-TPC film (left) and Tb-TPC film (right). (c) X-ray images of the standard resolution test pattern plate based on the Eu-TPC film and Tb-TPC film, and the corresponding gray value analysis at a spatial resolution value of 4 lp mm^{-1}, which were marked with yellow lines. (d) X-ray images of a metallic spring in the capsule based on the Eu-TPC film and Tb-TPC film.

This journal is © The Royal Society of Chemistry 2023

J. Mater. Chem. C, 2023, **11**, 7405–7410 | **7409**

References

1 P. Büchele, M. Richter, S. F. Tedde, G. J. Matt, G. N. Ankah, R. Fischer, M. Biele, W. Metzger, S. Lilliu, O. Bikondoa, J. E. Macdonald, C. J. Brabec, T. Kraus, U. Lemmer and O. Schmidt, *Nat. Photonics*, 2015, **9**, 843–848.

2 H. M. Thirimanne, K. Jayawardena, A. J. Parnell, R. M. I. Bandara, A. Karalasingam, S. Pani, J. E. Huerdler, D. G. Lidzey, S. F. Tedde, A. Nisbet, C. A. Mills and S. R. P. Silva, *Nat. Commun.*, 2018, **9**, 2926.

3 M. J. Weber, *J. Lumin.*, 2002, **100**, 35–45.

4 N. Gan, X. Zou, M. Dong, Y. Wang, X. Wang, A. Lv, Z. Song, Y. Zhang, W. Gong, Z. Zhao, Z. Wang, Z. Zhou, H. Ma, X. Liu, Q. Chen, H. Shi, H. Yang, L. Gu, Z. An and W. Huang, *Nat. Commun.*, 2022, **13**, 3995.

5 M. Gandini, I. Villa, M. Beretta, C. Gotti, M. Imran, F. Carulli, E. Fantuzzi, M. Sassi, M. Zaffalon, C. Brofferio, L. Manna, L. Beverina, A. Vedda, M. Fasoli, L. Gironi and S. Brovelli, *Nat. Nanotechnol.*, 2020, **15**, 462–468.

6 X. Wang, H. Shi, H. Ma, W. Ye, L. Song, J. Zan, X. Yao, X. Ou, G. Yang, Z. Zhao, M. Singh, C. Lin, H. Wang, W. Jia, Q. Wang, J. Zhi, C. Dong, X. Jiang, Y. Tang, X. Xie, Y. Yang, J. Wang, Q. Chen, Y. Wang, H. Yang, G. Zhang, Z. An, X. Liu and W. Huang, *Nat. Photonics*, 2021, **15**, 187–192.

7 J.-X. Wang, I. Dutta, J. Yin, T. He, L. Gutiérrez-Arzaluz, O. M. Bakr, M. Eddaoudi, K.-W. Huang and O. F. Mohammed, *Matter*, 2023, **6**, 217–225.

8 J.-X. Wang, L. Gutiérrez-Arzaluz, X. Wang, T. He, Y. Zhang, M. Eddaoudi, O. M. Bakr and O. F. Mohammed, *Nat. Photonics*, 2022, **16**, 869–875.

9 F. P. Doty, C. A. Bauer, A. J. Skulan, P. G. Grant and M. D. Allendorf, *Adv. Mater.*, 2009, **21**, 95–101.

10 J. Lu, J. Gao, W.-F. Wang, B.-Y. Li, P.-X. Li, F.-K. Zheng and G.-C. Guo, *J. Mater. Chem. C*, 2021, **9**, 5615–5620.

11 J. Lu, S. H. Wang, Y. Li, W. F. Wang, C. Sun, P. X. Li, F. K. Zheng and G. C. Guo, *Dalton Trans.*, 2020, **49**, 7309–7314.

12 J. Lu, X. H. Xin, Y. J. Lin, S. H. Wang, J. G. Xu, F. K. Zheng and G. C. Guo, *Dalton Trans.*, 2019, **48**, 1722–1731.

13 J. Lu, X.-H. Zhao, B. Bai, F.-K. Zheng and G.-C. Guo, *J. Mater. Chem. C*, 2019, **7**, 11099–11103.

14 S. R. Mathis, Ii, S. T. Golafale, J. Bacsa, A. Steiner, C. W. Ingram, F. P. Doty, E. Auden and K. Hattar, *Dalton Trans.*, 2017, **46**, 491–500.

15 C. Wang, O. Volotskova, K. Lu, M. Ahmad, C. Sun, L. Xing and W. Lin, *J. Am. Chem. Soc.*, 2014, **136**, 6171–6174.

16 J.-X. Wang, L. Gutiérrez-Arzaluz, X. Wang, M. Almalki, J. Yin, J. Czaban-Józwiak, O. Shekhah, Y. Zhang, O. M. Bakr, M. Eddaoudi and O. F. Mohammed, *Matter*, 2022, **5**, 253–265.

17 Y. Wang, X. Yin, W. Liu, J. Xie, J. Chen, M. A. Silver, D. Sheng, L. Chen, J. Diwu, N. Liu, Z. Chai, T. E. Albrecht-Schmitt and S. Wang, *Angew. Chem., Int. Ed.*, 2018, **57**, 7883–7887.

18 J. Gao, J. Lu, B. Li, W. Wang, M. Xie, S. Wang, F. Zheng and G. Guo, *Chin. Chem. Lett.*, 2022, **33**, 5132–5136.

19 X. Zhang, H. Qiu, W. Luo, K. Huang, Y. Chen, J. Zhang, B. Wang, D. Peng, Y. Wang and K. Zheng, *Adv. Sci.*, 2023, 2207004.

20 J. Perego, I. Villa, A. Pedrini, E. C. Padovani, R. Crapanzano, A. Vedda, C. Dujardin, C. X. Bezuidenhout, S. Bracco, P. E. Sozzani, A. Comotti, L. Gironi, M. Beretta, M. Salomoni, N. Kratochwil, S. Gundacker, E. Auffray, F. Meinardi and A. Monguzzi, *Nat. Photonics*, 2021, **15**, 393–400.

21 A. A. Kukinov, T. V. Balashova, V. A. Ilichev, A. N. Trufanov, M. N. Ivin, S. V. Obolensky and M. N. Bochkarev, *Phys. Chem. Chem. Phys.*, 2019, **21**, 16288–16292.

22 M. J. Neufeld, H. Winter, M. R. Landry, A. M. Goforth, S. Khan, G. Pratx and C. Sun, *ACS Appl. Mater. Interfaces*, 2020, **12**, 26943–26954.

23 W.-F. Wang, J. Lu, X.-M. Xu, B.-Y. Li, J. Gao, M.-J. Xie, S.-H. Wang, F.-K. Zheng and G.-C. Guo, *Chem. Eng. J.*, 2022, **430**, 133010.

24 X. Wang, Y. Wang, Y. Wang, H. Liu, Y. Zhang, W. Liu, X. Wang and S. Wang, *Chem. Commun.*, 2019, **56**, 233–236.

25 W. Ma, Y. Su, Q. Zhang, C. Deng, L. Pasquali, W. Zhu, Y. Tian, P. Ran, Z. Chen, G. Yang, G. Liang, T. Liu, H. Zhu, P. Huang, H. Zhong, K. Wang, S. Peng, J. Xia, H. Liu, X. Liu and Y. M. Yang, *Nat. Mater.*, 2022, **21**, 210–216.

26 F. Zhang, Y. Zhou, Z. Chen, M. Wang, Z. Ma, X. Chen, M. Jia, D. Wu, J. Xiao, X. Li, Y. Zhang, Z. Shi and C. Shan, *Adv. Mater.*, 2022, **34**, 2204801.

27 E. G. Moore, A. P. S. Samuel and K. N. Raymond, *Acc. Chem. Res.*, 2009, **42**, 542–552.

28 F. Chen, Z. Chen, Z. Bian and C. Huang, *Coord. Chem. Rev.*, 2010, **254**, 991–1010.

29 X. Ou, X. Qin, B. Huang, J. Zan, Q. Wu, Z. Hong, L. Xie, H. Bian, Z. Yi, X. Chen, Y. Wu, X. Song, J. Li, Q. Chen, H. Yang and X. Liu, *Nature*, 2021, **590**, 410–415.

30 C. Wei, L. Ma, H. Wei, Z. Liu, Z. Bian and C. Huang, *Sci. China Technol. Sci.*, 2018, **61**, 1265–1285.

31 H. Xu, Q. Sun, Z. An, Y. Wei and X. Liu, *Coord. Chem. Rev.*, 2015, **293–294**, 228–249.

32 M. Latva, H. Takalo, V.-M. Mukkala, C. Matachescu, J. C. Rodríguez-Ubis and J. Kankare, *J. Lumin.*, 1997, **75**, 149–169.

33 X. Liu, Y. Jiang, F. Li, X. Xu, R. Li, W. Zhu, J. Ni, C. Ding, S. Liu and Q. Zhao, *Adv. Opt. Mater.*, 2022, 2202169.

34 X. Liu, R. Li, X. Xu, Y. Jiang, W. Zhu, Y. Yao, F. Li, X. Tao, S. Liu, W. Huang and Q. Zhao, *Adv. Mater.*, 2022, 2206741.

35 H. Lu, Z. Zheng, Z.-J. Li, H. Bao, X. Guo, X. Guo, J. Lin, Y. Qian and J.-Q. Wang, *ACS Appl. Mater. Interfaces*, 2021, **13**, 2745–2752.

36 T. Jiang, W. Ma, H. Zhang, Y. Tian, G. Lin, W. Xiao, X. Yu, J. Qiu, X. Xu, Y. Yang and D. Ju, *Adv. Funct. Mater.*, 2021, **31**, 2009973.

37 W. Ma, T. Jiang, Z. Yang, H. Zhang, Y. Su, Z. Chen, X. Chen, Y. Ma, W. Zhu, X. Yu, H. Zhu, J. Qiu, X. Liu, X. Xu and Y. M. Yang, *Adv. Sci.*, 2021, **8**, 2003728.

38 H. Zhang, Z. Yang, M. Zhou, L. Zhao, T. Jiang, H. Yang, X. Yu, J. Qiu, Y. M. Yang and X. Xu, *Adv. Mater.*, 2021, **33**, 2102529.